

# MS<sup>2</sup>3D: A 3D Object Detection Method Using Multi-Scale Semantic Feature Points to Construct 3D Feature Layer

Yongxin Shao, Aihong Tan, Tianhong Yan, Zhetao Sun

**Abstract**—Lidar point clouds, as a type of data with accurate distance perception, can effectively represent the motion and posture of objects in three-dimensional space. However, the sparsity and disorderliness of point clouds make it challenging to extract features directly from them. Many studies have addressed this issue by transforming point clouds into regular voxel representations. However, these methods often lead to the loss of fine-grained local feature information due to downsampling. Moreover, the sparsity of point clouds poses difficulties in efficiently aggregating features in 3D feature layer using voxel-based two-stage methods. To address these issues, this paper proposes a two-stage 3D detection framework called MS<sup>2</sup>3D. In MS<sup>2</sup>3D, we utilize small-sized voxels to extract fine-grained local features and large-sized voxels to capture long-range local features. Additionally, we propose a method for constructing 3D feature layer using multi-scale semantic feature points, enabling the transformation of sparse 3D feature layer into more compact representations. Furthermore, we compute the offset between feature points in the 3D feature layer and the centroid of objects, aiming to bring them as close as possible to the object's center. It significantly enhances the efficiency of feature aggregation. To validate the effectiveness of our method, we evaluated our method on the KITTI dataset and ONCE dataset together.

**Index Terms**—3D object detection, Point cloud, Lidar, Deep learning.

## I. INTRODUCTION

WITH the continuous development of artificial intelligence technologies, 2D object detection methods [1]–[8] have become highly mature. However, in autonomous driving scenarios, 2D object detection lacks depth information, making it difficult to accurately represent objects' motion and pose. Although subsequent 3D object detection methods using stereo cameras [9]–[12] or depth cameras [13]–[16] can describe the pose of objects in three-dimensional space, they are susceptible to lighting conditions and occlusions, often resulting in poor performance in complex outdoor scenes. In comparison, Lidar is unaffected by environmental lighting conditions and can provide point clouds that are more suitable for representing the position of objects in three-dimensional space [17]–[19].

However, point clouds possess specific characteristics [20] (sparsity, disorderliness, rotation invariance) that make direct feature extraction challenging. To address these issues, some

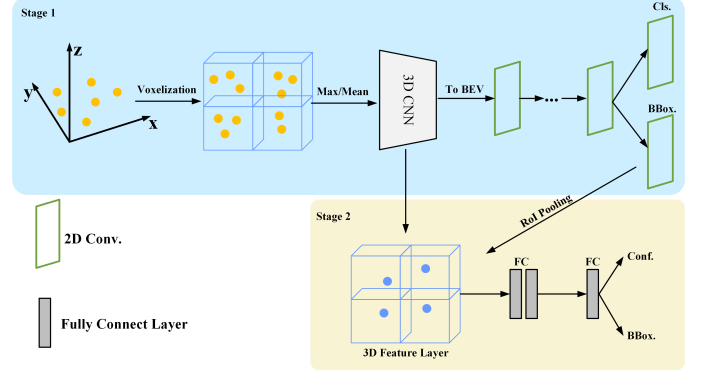


Fig. 1. Overview of voxel-based 3D object detection methods. The blue portion represents the basic workflow of one-stage methods, while the combination of the blue and yellow portions represents the basic workflow of two-stage methods.

methods convert point clouds into regular voxel representations and utilize 3D convolutions for feature extraction. Fig. 1 illustrates the basic structure of voxel-based methods. Voxel-based methods can be categorized into one-stage and two-stage methods. In one-stage methods [21], [22], the point clouds are voxelized, then the mean or maximum value of the feature points within each voxel is computed. Subsequently, a 3D convolutional neural network (CNN) is employed for feature extraction. The resulting features are transformed into bird's-eye view feature maps, and object detection is performed from that perspective. Two-stage methods [23] utilize the bounding boxes detected in the first stage as region proposals. These region proposals are then used to aggregate feature information on the 3D feature layer to accomplish the final detection task. While voxel-based methods have achieved promising results, there are still some issues that need to be addressed: (1) Multiple downsampling of voxels of a single size can lead to the loss of fine-grained local features; (2) Compared to images, point clouds generated by Lidar have lower resolution and sparser distribution. The operations of mean or taking maximum values of feature points within each voxel, as well as downsampling during the feature extraction process, further exacerbate the sparsity of the original point cloud; (3) Point clouds mainly exist on the surface of objects, and the centroids of objects are often distant from any point cloud.

In this paper, we propose a method called MS<sup>2</sup>3D, which improves the above problem by constructing a 3D feature layer using multi-scale semantic feature points. Firstly, we

Yongxin Shao, Aihong Tan, Tianhong Yan, and Zhetao Sun are with the School of Mechanical and Electrical Engineering, China Jiliang University, Hanzhou, 310018, China. (email: syx1536505936@163.com; Tanah@cjlu.edu.cn; thyan@163.com; zhetaosun@163.com). Aihong Tan and Tianhong Yan are the Corresponding Author.

propose the Multi-Scale Voxelization module, which extracts fine-grained local features using small-sized voxels and long-range features with a large receptive field using large-sized voxels. Secondly, we construct a relatively dense 3D feature layer using feature points with different scales of semantic information from different levels. Thirdly, motivated by VoteNet [24], we perform Center Vote operations on deep-level feature points in the constructed 3D feature layer to make these points as close as possible to the object's centroid. Meanwhile, for shallow-level feature points, we aim to retain them near the object's surface and preserve the object's geometric shape in the 3D feature layer. In the Multi-Scale Voxelization, we propose a distance-weighted mean operation to assign larger feature weights to feature points closer to the object's centroid. The distance-weighting is also used to pick out foreground points close to the object's centroid. The main contributions of this paper are as follows:

- Utilizing voxels of different sizes to extract feature information at different granularities.
- Proposed a method to construct a relatively dense and semantically rich 3D feature layer that adequately represents the object's geometric shape.
- Conducting experiments on the KITTI and ONCE datasets to evaluate the proposed method, demonstrating its strong performance even on large-scale datasets with complex environments.

## II. RELATED WORK

The methods for 3D object detection based on Lidar point clouds are categorized according to their data representation formats: voxel-based, point-based, and projection-based methods. Additionally, there are also fusion methods that combine voxel-based and point-based methods.

### A. Voxel-based Method

Voxel-based methods typically convert point clouds into regular voxel representations and perform a series of feature extractions using 3D CNN. VoxelNet, proposed by Zhou et al. [22], is a one-stage detection method based on voxel. It encodes the transformed voxels using a Voxel Feature Encoder (VFE) and feeds them into a 3D CNN for feature extraction, ultimately completing the detection task from a bird's-eye view perspective. Subsequently, Guo et al. [21] proposed SECOND, which improves the detection efficiency of VoxelNet by introducing sparse convolution for feature extraction. SA-SSD, proposed by He et al. [25], strengthens the network's perception of point cloud structural information by introducing an auxiliary network. CIA-SSD, proposed by Zheng et al. [26], combines deep semantic information with shallow spatial information by introducing the Spatial-Semantic Feature Aggregation (SSFA) module. HVNet, proposed by Ye et al. [27], aggregate and project the multi-scale feature maps to achieve better performance. Voxel RCNN, proposed by Deng et al. [23], proposes the Voxel RoI Pooling module to refine the region proposals from the first stage by aggregating 3D features in the 3D feature layer. PartA<sup>2</sup>, proposed by Shi et al. [28], consists of part perception and aggregation modules to

enhance the network's detection accuracy by perceiving object part distributions.

### B. Point-based Method

Unlike voxel-based methods, point-based methods typically utilize PointNet [20] and its variants [29]–[32] for feature extraction. Point RCNN, proposed by Shi et al. [33], is a two-stage detection method based on point. In the first stage, foreground points obtained through segmentation are used to generate region proposals. In the second stage, semantic features and local spatial features are utilized to refine the region proposals. VoteNet, proposed by Qi et al. [24], proposes a deep Hough voting module for predicting instance centers and has achieved promising results. 3DSSD, proposed by Yang et al. [34], reduces computational costs by removing all upsampling modules and proposes a fusion sampling method, enabling detection on less representative points. IA-SSD, proposed by Zhang et al. [35], proposes two learnable, task-oriented instance-aware subsampling strategies that hierarchically select foreground points belonging to object-relevant regions of interest.

### C. Projection-based Method

Projection-based methods commonly project point clouds onto a single or multiple view, transforming them into structured 2D pseudo-image representations, which are then subjected to feature extraction using 2D CNNs. MV3D, proposed by Chen et al. [36], translates point clouds into bird's-eye view and perspective view representations, extracting point cloud features and subsequently fusing features with corresponding scene images. AVOD, proposed by Ku et al. [37], eliminates the input of the perspective view. Complex YOLO and YOLO3D [38], [39] conduct feature extraction and subsequent detection tasks from the bird's-eye view. PointPillars, proposed by Lang et al. [40], encodes point clouds from bird's-eye view into top-down pillars with high-dimensional features using the voxel feature encoding method and then employs 2D CNNs to accomplish subsequent tasks. H<sup>2</sup>3D RCNN by Deng et al. [41] employs a similar feature encoding method to PointPillars, effectively utilizing features from bird's-eye view and perspective view to obtain region proposals using 2D CNNs. Subsequently, 3D feature layer are generated from features in bird's-eye view and perspective view, which were then used to refine the region proposals subsequently.

### D. Voxel & Point-based Method

To overcome the limitations of voxel-based and point-based methods [42], some methods have started to use voxel-point representations for 3D detection tasks. PV-RCNN, proposed by Shi et al. [43], combines the efficient feature extraction of 3D voxel CNN with the flexible receptive field of point-based networks, achieving promising results. HVPR, proposed by Noh et al. [44], proposes an efficient memory module to enhance point-based features, striking a good balance between accuracy and efficiency. BADet, proposed by Qian et al. [45], constructs a lightweight region aggregation network through local neighborhood graphs to achieve more accurate bounding box predictions.

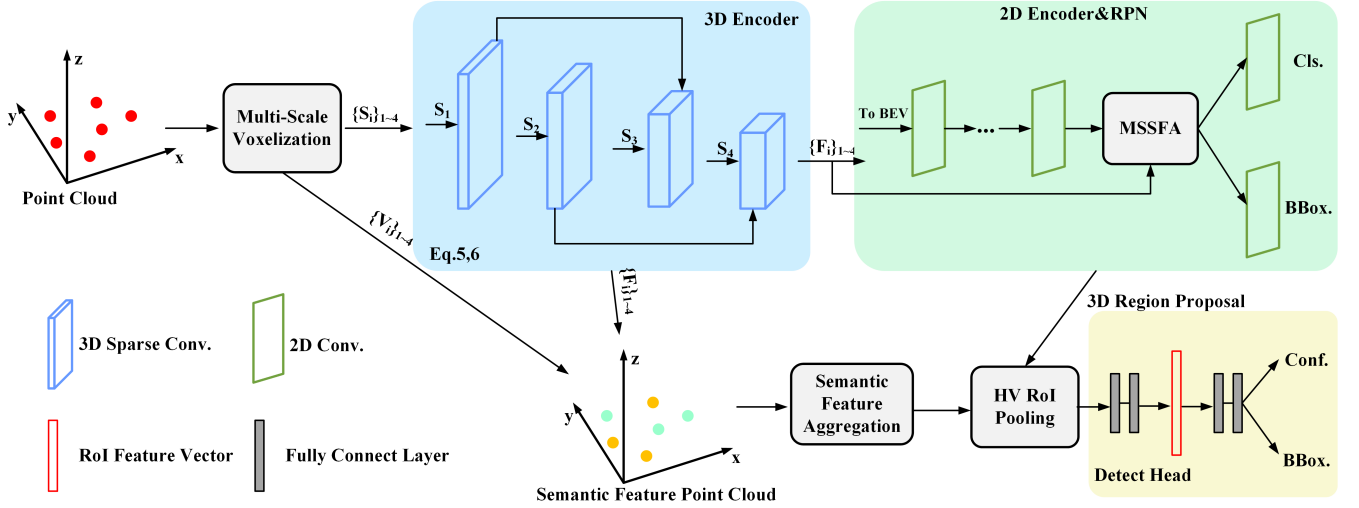


Fig. 2. Overview of the MS<sup>2</sup>3D structure.  $\{S_i\}_{i=1-4}$  represents the Sparse Voxel Features of different sizes generated by the Multi-Scale Voxelization from the input raw point cloud.  $\{F_i\}_{i=1-4}$  represents the Sparse Voxel Features generated by the 3D encoder.  $\{V_i\}_{i=1-4}$  represents the Voxel-wise Features generated by the Multi-Scale Voxelization.

### III. METHODOLOGY

In this section, we will introduce the specific structure of MS<sup>2</sup>3D and the corresponding design of the loss function. MS<sup>2</sup>3D is a two-stage 3D object detection framework based on voxel. As shown in Fig. 2, MS<sup>2</sup>3D consists of the following components: (1) Multi-Scale Voxelization, (2) 3D encoder, (3) 2D encoder, and (4) Semantic Feature Aggregation. Multi-scale voxelization divides the input raw point cloud into voxel grids of different scales and feeds them into a 3D encoder for feature extraction. Then, the sparse voxel features are transformed into bird's eye view representation, and 3D region proposals are generated using the 2D encoder and Region Proposal Network (RPN). In the 2D encoder, we adopt the Multi-layer Spatial-Semantic Feature Aggregation (MSSFA) module proposed in our previous work PV-SSD [46], which is used to interact local and global features. Subsequently, we integrate the sparse voxel features generated by the Multi-Scale Voxelization and 3D encoder to generate a Semantic Feature Point Cloud and perform Semantic Feature Aggregation, constructing the 3D feature layer. Lastly, we employ the Hierarchical Voxel RoI Pooling (HV RoI Pooling) proposed in H<sup>2</sup>3D R-CNN to aggregate RoI features and refine the previous 3D region proposals.

#### A. Multi-Scale Voxelization

In the process of point cloud voxelization, smaller voxel sizes can preserve more local detail information but lack a larger perception range. Using 3D convolution for downsampling to improve the perception range may result in losing local details. To address this issue, we propose Multi-Scale Voxelization to generate sparse voxel features of different voxel sizes. Extracting multi-scale features also facilitates the generation of finer-grained positional features. Furthermore, we utilize them to construct 3D feature layer with richer semantic information.

During the Multi-Scale Voxelization process, we voxelize the raw point cloud based on voxel sizes  $\{s_i\}_{i=1-4}$  (It should be noted that in the voxel encoding process, random sampling and zero-padding operations in hard voxelization [22] can cause the loss of a significant amount of point cloud information and result in an uncertain number of embedded point clouds. In MS<sup>2</sup>3D, we adopt dynamic voxel encoding [47]). Feature encoder is performed to obtain Sparse Voxel Features  $\{S_i\}_{i=1-4}$  and Voxel-wise Features  $\{V_i\}_{i=1-4}$  (We set four different sizes,  $i \in [1, 4]$ . Multi-Scale Voxelization involves voxelizing four times, with each voxel size doubling.) After each voxelization, the perception range of the feature points within the voxels is expanded. Shallow-level feature points have better perception capabilities for cyclists and pedestrians, while deep-level feature points have better perception capabilities for cars. Finally, these feature points with different perception ranges and levels of semantic information are aggregated through Semantic Feature Aggregation to form a densely 3D feature layer with rich semantic information. The specific feature encoding method is illustrated in Fig. 3.

We define the point cloud features input to the feature encoder as comprised of coordinate feature  $C \in R^{N \times 10}$  and point feature  $P \in R^{N \times C_{in}}$  (where  $N$  represents the number of points and  $C'$  represents the number of feature). The coordinate feature is a 10-dimensional vector:  $(x, y, z, r, x_c, y_c, z_c, x_p, y_p, z_p)$ . Here,  $x, y, z, r$  denote the 3D coordinates and reflectance intensity of the point cloud, while  $x_c, y_c, z_c$  represent the geometric center of all points in the voxel containing the point cloud, and  $x_p, y_p, z_p$  denote  $x - x_c, y - y_c, z - z_c$ , respectively, indicating the point's relative position to the geometric center. To enhance the features, we apply two fully connected network (FCN) layers to expand the dimensions of  $C$  and  $P$ , followed by a concatenation operation in the feature dimension, resulting in the Point-wise Feature. Subsequently, a max operation is applied to the Point-wise Feature, followed by a concatenation operation,

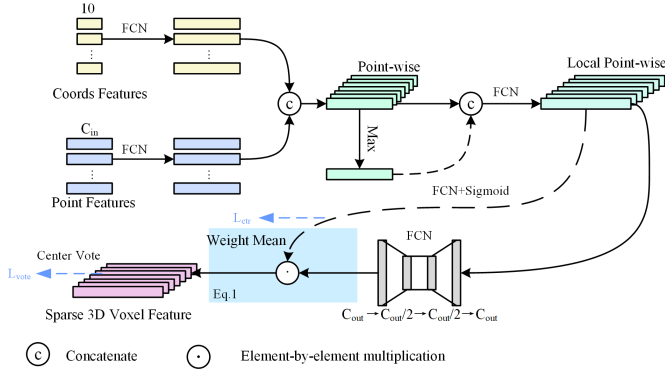


Fig. 3. Overview of the structure of the feature encoding process in Multi-Scale Voxelization. The Center Vote operation and the calculation of  $L_{vote}$  are only applied in the Multi-Scale Voxelization with the largest voxel size. The blue region in the figure represents the Weight Mean module.

resulting in the Local Point-wise Feature  $P_{local} \in R^{N \times C'}$ . By using an FCN followed by a Sigmoid function, a distance weight  $W_d \in R^{N \times 1}$  is generated to describe the distance of each point from the object center ( $W_d \in [0, 1]$ , with values proximity to 1 indicating closer to the object center). The  $P_{local}$  is integrated using two FCN layers. In the Weight Mean module, we perform element-wise multiplication between  $W_d$  and the integrated  $P_{local}$ , resulting in Voxel-wise Feature  $V_i \in R^{N \times C_{out}}$ . Subsequently, for  $V_i$  with the same voxel index, we perform the mean operation to obtain  $S_i$ . We then select the top K  $V_i$  with the highest weights based on the previously obtained  $W_d$ . These selected features become the input for the next Multi-Scale Voxelization module. In autonomous driving scenarios, the point cloud data often contains a significant number of background points. For the task of 3D object detection, it is crucial to prioritize the point cloud features closer to the objects' center. The Weight Mean operation is a weighted average operation that assigns greater attention to the point cloud features closer to the object center. The coordinates of  $V_i$  (indexed from 1 to 4) are defined as  $X_i \in R^{N \times 3}$ . The equation for the Weight Mean operation is shown as (1).

$$mean_w(x, W_d, X_V) = mean(W_d \cdot x, X_V) \quad (1)$$

Furthermore, motivated by VoteNet [24], we want to bring feature points with rich semantic information closer to the object's center. Therefore, in the final layer of the Multi-Scale Voxelization feature encoder, we incorporate the Center Vote operation, predicting the offset of Voxel-wise Features from the object's center. We use  $L_{vote}$  and  $L_{ctr}$  for supervising the prediction of center point offsets from the Center Vote as well as the prediction of  $W_d$ . The specific equation are presented as (2), (3), and (4).

$$Mask_i = \sqrt[3]{\frac{\min(f^*, b^*)}{\max(f^*, b^*)} \times \frac{\min(l^*, r^*)}{\max(l^*, r^*)} \times \frac{\min(u^*, d^*)}{\max(u^*, d^*)}} \quad (2)$$

$$L_{ctr} = -(Mask_i \cdot a_i \log(W_d) + (1 - a_i) \log(1 - W_d)) \quad (3)$$

$$L_{vote}^v = \frac{1}{M_{pos}} \sum \|\Delta x_i - \Delta \hat{x}_i\| \quad (4)$$

Where  $f^*, b^*, l^*, r^*, u^*, d^*$  respectively denote the distances of feature points to the six surfaces (front, back, left, right, up, and down) of the ground truth bounding box.  $a_i$  denotes the one-hot encoding of foreground and background points in the point cloud.  $M_{pos}$  denotes the count of foreground points.  $\Delta x_j \in R^3$  denotes the object's center point, while  $\Delta \hat{x}_j \in R^3$  denotes the new coordinates of the feature points obtained by adding the predicted coordinate offsets. To prevent irrelevant background points from being shifted close to positive samples or even onto the object's interior, during the Center Vote process, we exclusively involve positive samples in the computation of  $L_{vote}^v$ .

### B. 3D Encoder

In the 3D encoder, we employ the sparse convolution proposed in SECOND [21] for further feature extraction on  $\{S_i\}_{1-4}$ . Here we define  $\{f_i\}_{1-4}$  as the sparse convolution corresponding to  $\{S_i\}_{1-4}$ . To optimize computational efficiency in the subsequent 2D encoder, we perform various levels of downsampling on  $S_i$ . Specifically,  $S_1$  and  $S_2$  undergo a 4x downsampling, while for  $S_3$ , we perform a 4x downsampling in the W and H dimensions and a 2x downsampling in the D dimension. For  $S_4$  we apply a 4x downsampling in the W and H dimensions, but no downsampling in the D dimension (note that during the computation of sparse convolution,  $S_i$  is reconstructed, where  $S_i \in R^{W \times H \times D \times C}$ ). Furthermore, to enrich the acquired semantic features, we feed the outputs of  $f_1(x)$  and  $f_2(x)$  into  $f_3(x)$  and  $f_4(x)$  respectively, and concatenate them with the outputs of  $f_3(x)$  and  $f_4(x)$ . The ultimate output is defined as  $\{F_i\}_{1-4} \in R^{N \times 2C_{out}}$ . The process of the 3D encoder's feature encoding is as follows.

$$F_{1,2} = f_{1,2}(S_{1,2}) \quad (5)$$

$$\{F_i\}_{3,4} = Cat(F_{1,2}, f_{3,4}(S_{3,4})) \quad (6)$$

### C. 2D Encoder

In the 2D encoder, we initially transform  $\{F_i\}_i$  into feature maps under the bird's eye view, followed by further feature extraction using 2D convolutions for generating region proposals from bird's eye view in the subsequent steps.

As illustrated in Fig. 4(b), we define the 2D feature obtained by N Base Blocks as  $B'_i \in R^{W' \times H' \times C'}$ . Subsequently,  $B'_i$  undergoes two  $3 \times 3$  convolution layers and a  $1 \times 1$  convolution layer for 2x downsampling, producing downsampled 2D feature  $D_i \in R^{\frac{W'}{2} \times \frac{H'}{2} \times C'}$  (no downsampling is performed for  $i = 4$ ). Additionally, we concatenate the output  $D_{i-1}$  from the previous layer with  $B'_i$  to ensure that the output feature encompasses richer semantic information. Finally, feature integration is performed using a  $1 \times 1$  convolution layer and a  $3 \times 3$  convolution layer, resulting in the 2D bird's eye view features  $\{B_i\}_{1-4} \in R^{W' \times H' \times C'}$ .

For the Base Block in the 2D encoder, we designed a feature encoding structure with two dimensions of spatial and features. As illustrated in Fig. 4(a), the Base Block comprises the  $1 \times 1$  branch,  $3 \times 3$  branch, and residual branch. The  $1 \times 1$



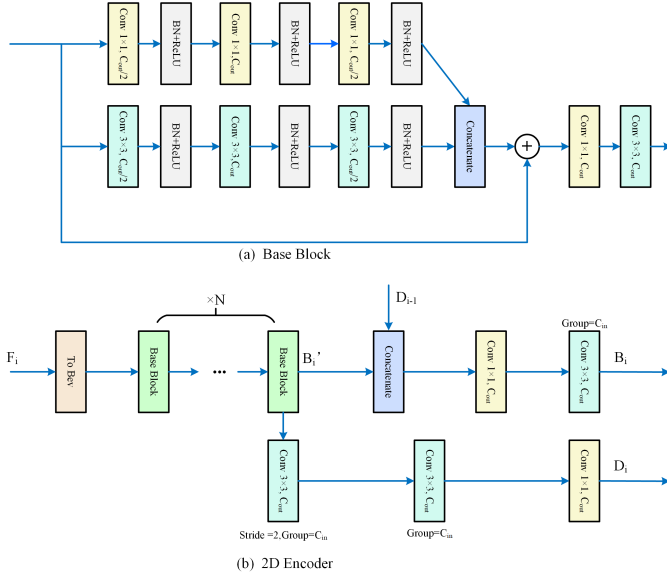


Fig. 4. Overview of the structure of the 2D encoder. In (a), the architecture of the Base Block within the 2D encoder is illustrated. Here, BN represents Batch Normalization operation. In (b), the complete structure of the 2D encoder is illustrated. It's important to note that when  $i = 4$ , there is no downsampling branch.

branch integrates features across the feature dimension of the 2D feature map, while the  $3 \times 3$  branch integrates features across the spatial dimension to extract local features between neighboring pixels. The outputs of the  $1 \times 1$  and  $3 \times 3$  branches are concatenated and element-wise added to the output of the residual branch. Subsequently, further feature integration is conducted through a  $1 \times 1$  convolution layer and a  $3 \times 3$  convolution layer. The  $1 \times 1$  and  $3 \times 3$  branches consist of three sets of Convolution + ReLU + Batch Normalization combinations.

#### D. Semantic Feature Aggregation

At present, the resolution of Lidar is weaker compared to the camera, which often makes it challenging to depict the outlines of small objects, especially in the 3D feature layer (before box refinement, the 3D features are aggregated to form the 3D feature layer). Due to voxelization, the features in the 3D feature layer are sparser. To address this issue, we propose Semantic Feature Aggregation to construct a relatively dense 3D feature layer using semantic feature points generated during the feature encoding process at various levels. As depicted in Fig. 5, the semantic point cloud aggregated from different levels of semantic features is denser than the raw point cloud, enabling better depiction of object contours (thanks to the Center Vote operation on the last layer of feature points in the Multi-Scale Voxelization module, as well as the implicit small-scale feature point shifts caused during voxel coordinate transformation, there is no occurrence of a large number of feature points sharing the same coordinates). Even after voxelization, the resulting sparse semantic voxel retains more details than the raw point cloud. Furthermore, as Lidar scans cover only the surfaces of objects, the object's center of mass tends to be away from its surface [24], [41]. It makes

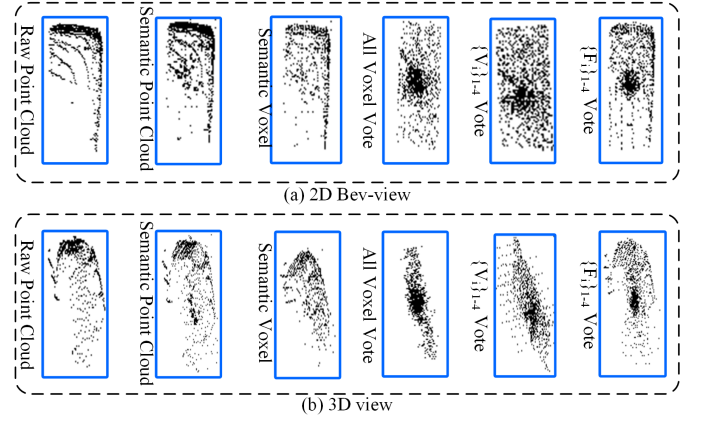


Fig. 5. Overview of semantic point cloud and the three Center Vote schemes. In (a), the result is visualized under the bird's-eye view, while in (b), the result is visualized in a 3D perspective. 'All Voxel Vote' denotes performing Center Vote for all semantic voxels. ' $\{V_i\}_{1-4}$  Vote' represents Center Vote applied to the sparse voxel features encoded through Multi-Scale Voxelization. ' $\{F_i\}_{1-4}$  Vote' represents Center Vote applied to the sparse voxel features encoded through the 3D encoder. 'Semantic Point Cloud' represents the set of feature points constructed with different scales of semantic feature points. 'Semantic Voxel' represents the Segment Point Cloud after voxelization.

difficult to accurately regress the bounding box from the RPN during box refinement. Motivated by VoteNet [24], we use the Center Vote operation to the voxelized semantic voxel to predict the offset from the center point. It allows the semantic voxel to approximate the object's center of mass as closely as possible. We propose three schemes for Center Vote (scheme (3) is the one used in MS<sup>2</sup>3D):

- Center Vote for all semantic voxels
- Center Vote only for  $\{V_i\}_{1-4}$  encoded through Multi-Scale Voxelization.
- Center Vote only for  $\{F_i\}_{1-4}$  encoded through the 3D encoder.

Visualization of the 3D feature layer constructed using these three schemes is presented in Fig. 5. From Fig. 5(a), we observe that when performing Center Vote for all semantic voxels, most feature points in the constructed 3D feature layer are concentrated around the object's center of mass. However, as depicted in Fig. 5(b), the 3D feature layer from a 3D perspective compresses in the vertical direction near the plane of the object's center of mass. While this aids subsequent HV RoI Pooling in aggregating features, it causes the 3D point cloud in the feature layer to lose the original geometric shape of the object. When performing Center Vote only for  $\{V_i\}_{1-4}$  the 3D feature layer, although relatively dispersed in the vertical direction, still cannot accurately capture the object's geometry. By performing Center Vote only for  $\{F_i\}_{1-4}$ , the 3D feature layer aggregates feature points near the object's center of mass while effectively depicting the object's geometry. Moreover,  $\{F_i\}_{1-4}$  are sparse voxel features encoded by a deep network, possessing rich semantic information, whereas  $\{V_i\}_{1-4}$  are sparse voxel features encoded by a shallow network, retaining the object's spatial geometric characteristics. This construction of the 3D feature layer is more favorable for subsequent box refinement. In the ablation experiment, we also conduct ablation experiments on these three schemes. Note that for

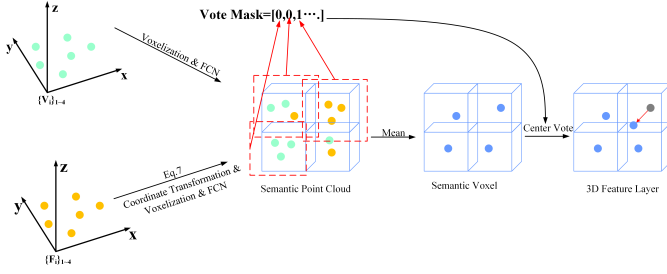


Fig. 6. Overview of Semantic Feature Aggregation Structure. In the 3D feature layer, the red arrows signify the offsets generated by the Center Vote, with the gray points denoting the original positions and the blue points indicating the positions after the offsets are applied.

scheme (2) and scheme (3), after voxelization, some voxels may simultaneously contain  $\{V_i\}_{1-4}$  and  $\{F_i\}_{1-4}$ . In fact, we only perform the center voting operation on voxels that contain only  $\{V_i\}_{1-4}$  or  $\{F_i\}_{1-4}$ .

Fig. 6 illustrates the structure of Semantic Feature Aggregation. Let's denote the coordinates of  $\{F_i\}_{1-4}$  as  $X'_F \in R^{N \times 3}$ , where  $X'_F$  are coordinates in the voxel coordinate system. On the other hand, the coordinates of  $\{V_i\}_{1-4}$  are  $X_V$  in the world coordinate system. First, we transform  $X'_F$  back to the world coordinate system using the coordinates of each voxel's center point, resulting in  $X_F \in R^{N \times 3}$ . The coordinate transformation formula is given by (7). Subsequently, we adjust  $\{F_i\}_{1-4}$  and  $\{V_i\}_{1-4}$  to have the same feature dimension through two FCN layers, followed by concatenation to generate the Semantic Point Cloud. Then, for feature points in the generated Semantic Point Cloud with the same voxel index, we perform a mean operation to obtain Semantic Voxel. Additionally, after generating the Semantic Point Cloud, we generate a mask  $Mask_{vote}$  based on whether a voxel contains  $\{V_i\}_{1-4}$  (0 if it contains  $\{V_i\}_{1-4}$ , 1 otherwise). This mask is used for subsequent Center Vote. After applying Center Vote using the mask to the Semantic Voxel, we obtain the final 3D feature layer. HV RoI Pooling is then used for 3D feature aggregation, followed by box refinement using FCN. The formulation for Semantic Feature Aggregation is provided in (8).

$$X_F = (X'_F + [0.5, 0.5, 0.5] \times V_{size} + \min(Range)) \quad (7)$$

$$F_{3D} = Vote(\text{mean}(\text{Cat}(FCN(\{V_i\}_{1-4}), FCN(\{F_i\}_{1-4})), X) \times Mask_{vote}) \quad (8)$$

Where  $V_{size} \in R^{1 \times 3}$  denotes the size of the voxel;  $\min(Range)$  denotes the minimum value of the range of the point cloud fed into the network;  $X = \{X_F, X_V\}$  denotes the coordinates of the Segment Point Cloud;  $FCN(x)$  denotes the Fully Connected Layer;  $Cat(x)$  denotes the Concatenate operation;  $\text{mean}(x)$  denotes the mean operation;  $Vote(x)$  is the Center Vote operation;  $F_{3D}$  denotes the 3D feature layer.

Furthermore, we have devised a loss function within the Semantic Feature Aggregation to supervise the offsets generated by the Center Vote. Similar to the approach mentioned in Multi-Scale Voxelization, this supervision solely applies to foreground points, excluding background points from contributing to the loss computation. However, in this context, we

solely compute the loss for foreground points where  $Mask_{vote}$  equals 1. The precise calculation formula is illustrated in (9).

$$L_{vote}^f = \frac{1}{M_{pos}} \sum Mask_{vote} \cdot a_i \|\Delta x_i - \hat{\Delta x}_i\| \quad (9)$$

### E. Loss Function

In the training phase, MS<sup>2</sup>3D uses end-to-end optimization, and the total loss function is calculated as shown in (10):

$$L_{total} = L_{rpn} + L_{head} + \alpha L_{vote} + \beta L_{ctr} \quad (10)$$

Where  $L_{rpn}$  is used to train the RPN [21], [22],  $L_{head}$  is used to train the detection head [23], and  $L_{vote}$  is used to train the Center Vote portion of Multi-Scale Voxelization feature encoding and Semantic Feature Aggregation.  $\alpha = 1, \beta = 0.25$ . The specific calculation equation is as follows:

$$L_{rpn} = \frac{1}{N_{fg}} \left[ L_{focal}(x_i, x_i^*) + \mathbb{K}(x_i^* > 1) \sum L_{loc}(y_i, y_i^*) \right] \quad (11)$$

$N_{fg}$  denotes foreground anchors;  $x_i$  and  $y_i$  denote the outputs of the categorization branch and the bounding box regression branch;  $x_i^*$  and  $y_i^*$  denote the labels of the corresponding categorization and bounding box regressions;  $\mathbb{K}(x_i^* > 1)$  denotes that only foreground anchors are involved in the computation of regression loss.  $L_{loc}$  is Smooth L1 Loss, and  $L_{focal}$  is Focal Loss.

In the detection head, the target confidence of the  $i$ th region proposal is calculated based on the Intersection over Union (IoU) of its corresponding ground-truth box:

$$r_i^*(IoU_i) = \begin{cases} 0 & IoU_i < \theta_l \\ \frac{IoU_i - \theta_l}{\theta_h - \theta_l} & \theta_l < IoU_i < \theta_h \\ 1 & IoU_i > \theta_h \end{cases} \quad (12)$$

Where  $\theta_h$  and  $\theta_l$  denote the IoU thresholds for foreground and background, respectively. The loss in the detection head section is calculated as follows:

$$L_{head} = \frac{1}{N_s} \left[ \sum L_{bce}(\gamma_i, \gamma_i^*(IoU_i)) + \mathbb{K}(IoU_i \geq \theta_{reg}) \sum L_{reg}(z_i, z_i^*) \right] \quad (13)$$

$L_{bce}$  denotes Binary Cross Entropy Loss;  $L_{reg}$  denotes Smooth L1 Loss;  $\gamma_i$  denotes the predicted value of confidence;  $z_i$  denotes the regression prediction of the detection head;  $N_s$  denotes the number of region proposals sampled.  $L_{vote}$  is computed as follows:

$$L_{vote} = L_{vote}^v + L_{vote}^f \quad (14)$$

## IV. EXPERIMENTS

### A. Datasets and Evaluation Metrics

**KITTI Dataset:** The KITTI dataset [48] is an open-source dataset designed for autonomous driving scenarios, encompassing road data collected from various sensors such as Lidar and camera. The dataset comprises 7,481 training samples and 7,518 testing samples. Among these, the training data is typically split into a training set of 3,712 samples and a validation set of 3,769 samples. In this paper, we

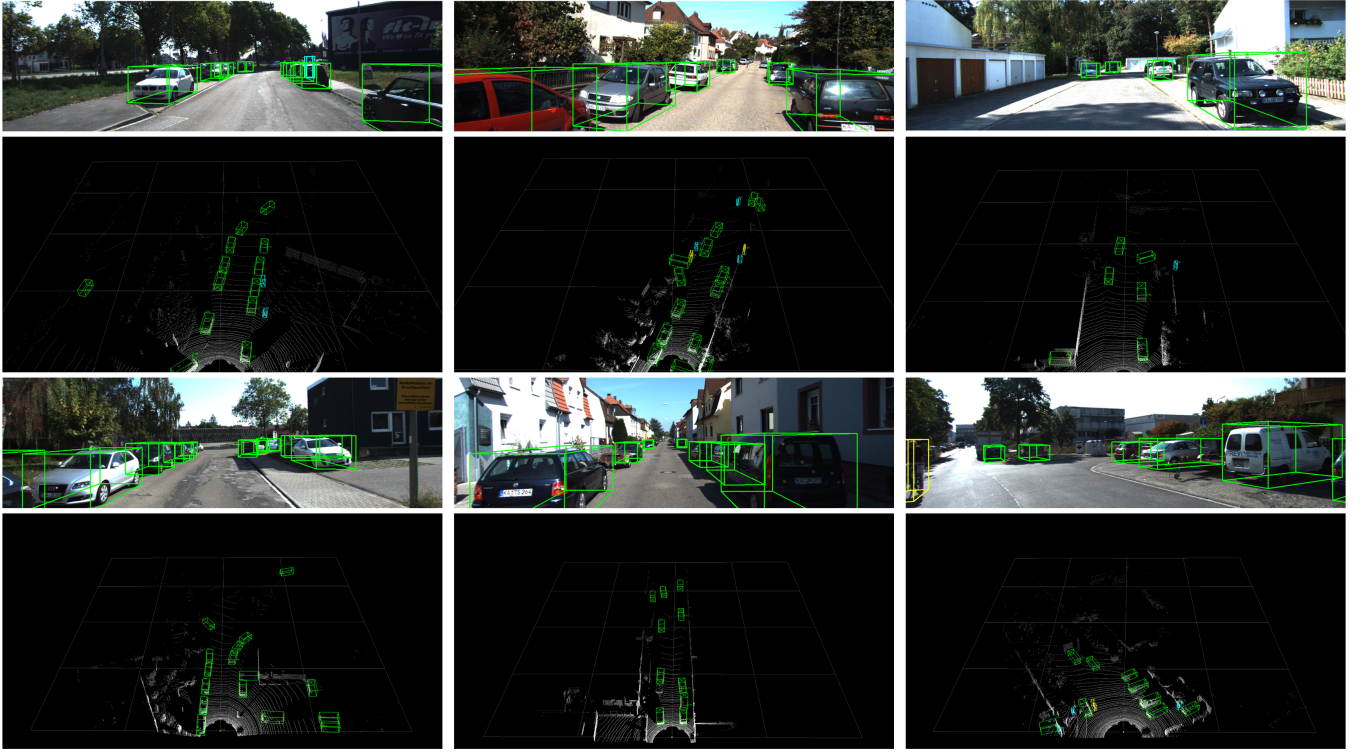


Fig. 7. Visualization of detection results on the KITTI dataset. The first and third rows show the detection outcomes projected onto images, while the second and fourth rows show the results on the point cloud. In these visualizations, the green bounding boxes correspond to ‘Car’, the yellow bounding boxes represent ‘Cyclist’, and the blue bounding boxes indicate ‘Pedestrian’.

randomly divide the training set into a training subset of 6,000 samples and a validation subset of 1,481 samples. The training subset is used for model training, while the validation subset aids in selecting the best-performing model. The ultimately chosen model is then evaluated on the KITTI testing set. Additionally, we utilize the data split of 3,712 training samples and 3,769 validation samples for ablation experiments. The KITTI dataset categorizes data into three difficulty levels (Easy, Moderate, Hard) based on object size, occlusion, and truncation factors.

**ONCE Dataset:** To further assess the effectiveness of our algorithm, we evaluate our method on the ONCE dataset [49]. This dataset comprises 6 sequences for training and 4 sequences for validation. We train our method on the training sequences and evaluate its performance on the validation sequences. The ONCE dataset categorizes objects into four evaluation levels (Overall,  $0 - 30m$  range objects,  $30 - 50m$  range objects, and  $> 50m$  range objects) based on their distance from the sensor. The evaluation uses Average Precision (AP) and Mean Average Precision (mAP) as the metrics.

### B. Implementation Details

**Voxelization:** For the KITTI dataset, we selected point clouds within the cartesian coordinate range of  $x = [0, 70.4]m$ ,  $y = [-40, 40]m$  and  $z = [-3.0, 1.0]m$ . The voxel size is set at  $(0.1m, 0.1m, 0.1m)$ . Following the approach in [47], we employed dynamic voxelization, which avoids random point discarding or zero-padding within voxels. For the ONCE dataset, we considered point clouds within the

cartesian coordinate range of  $x = [-73.6, 73.6]m$ ,  $y = [-73.6, 73.6]m$  and  $z = [-5.0, 3.0]m$ . The voxel size is set at  $(0.2m, 0.2m, 0.2m)$ .

**Data Augmentation:** We followed the methodology presented in SECOND [21] by randomly selecting objects from a constructed sample library and adding them to the current sample. For the KITTI dataset, we randomly selected 15 cars, 15 pedestrians, and 15 cyclists. For the ONCE dataset, we randomly selected 1 car, 1 bus, 3 trucks, 2 pedestrians, and 2 cyclists. Additionally, object instances underwent random rotation (with rotation angles selected from  $[-\pi/4, \pi/4]$ ), random scaling (scaling factors drawn from  $[0.95, 1.05]$ ), and random horizontal flipping along the x-axis [21], [22], [59].

**Network Architecture:** The feature encoding section of the Multi-Scale Voxelization employs the first and second FCN layers for feature dimension expansion. The subsequent FCN layers do not increase feature dimensions. The feature dimensions change as follows: first voxelization encoding ( $10 \rightarrow 16 \rightarrow 16$ ); second ( $16 \rightarrow 24 \rightarrow 24$ ); third ( $24 \rightarrow 24 \rightarrow 32$ ); fourth ( $32 \rightarrow 32 \rightarrow 48$ ). In the 2D encoder, each Base Block is repeated three times. The channel progression for the first two layers is ( $96 \rightarrow 128 \rightarrow 256$ ), and for the last two layers, it is ( $128 \rightarrow 128 \rightarrow 256$ ). HV RoI Pooling adheres to the same design as H<sup>2</sup>3D RCNN [41]. Region proposals are divided into coarse grids ( $3 \times 3 \times 3$ ) and fine grids ( $6 \times 6 \times 6$ ). The query radius is 6 for coarse grids and 3 for fine grids.

**Training:** The optimization algorithm employed is the one-cycle Adam [60], [61], with an initial learning rate of



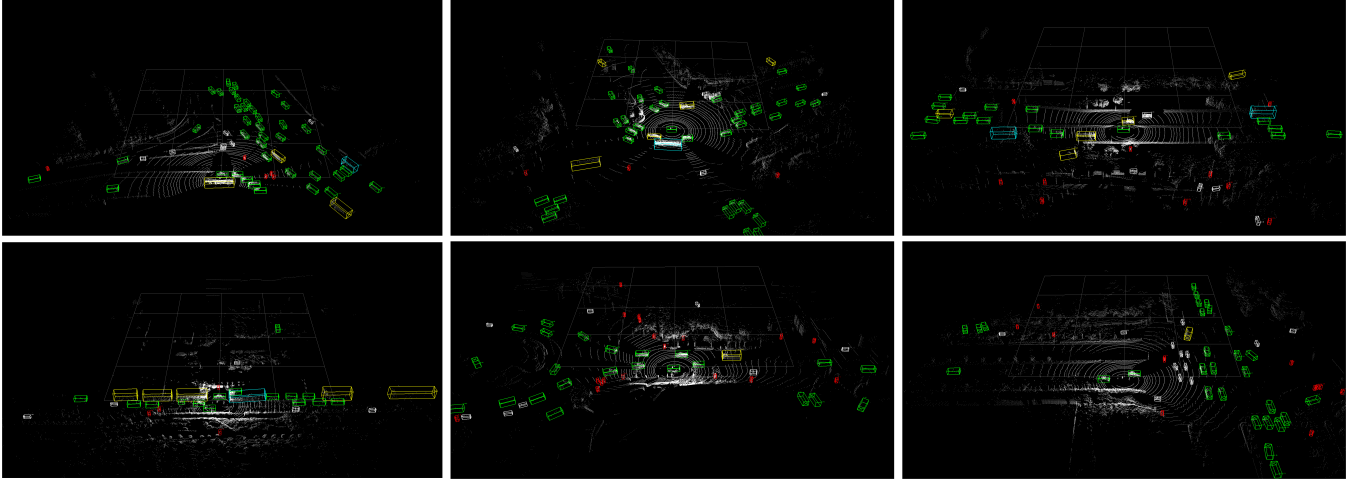


Fig. 8. Visualization of the detection results on the ONCE dataset. Yellow boxes represent ‘Truck’, green boxes represent ‘Car’, blue boxes represent ‘Bus’, red boxes represent ‘Pedestrian’, and white boxes represent ‘Cyclist’.

0.01, weight decay of 0.01, and momentum of 0.9. The IoU thresholds for foreground, background, and box regression in the detection head are set to 0.75, 0.25, and 0.55 (denoted as  $\theta_h$ ,  $\theta_l$ ,  $\theta_{reg}$ ). All implementations in this paper are based on the OpenPCDet<sup>1</sup> framework.

### C. Result on KITTI Dataset

We evaluated the 3D Average Precision (3D AP) for three categories: Car, Cyclist, and Pedestrian, with IoU thresholds of 0.7 for Car and 0.5 for Cyclist and Pedestrian. The detection results of our algorithm were submitted to the KITTI test dataset and are presented in Table I. In Table I, we classify 3D object detection methods based on point clouds into two categories: Lidar-based methods and fusion methods combining image and Lidar data. Additionally, Lidar-based methods are further categorized into three subtypes: (1) point-based, (2) voxel-based (considering that both voxel-based and projection-based methods transform a point cloud into a regular grid-like representation, in Table I, we categorize both types of methods as voxel-based), and (3) point & voxel-based. The proposed MS<sup>2</sup>3D in this paper falls into the voxel-based category, utilizing only point cloud data as input (it’s important to note that we adopted a multi-class joint training approach, where a single model was trained to detect objects from multiple classes). The final detection results were then submitted to the KITTI dataset. As shown in Table I, voxel-based methods tend to exhibit higher detection accuracy for the ‘Car’ category but lower accuracy for smaller objects such as ‘Cyclist’ and ‘Pedestrian’, which have fewer reflective points and smaller volumes. Conversely, our proposed algorithm demonstrates a relatively balanced detection accuracy across these three categories. This is attributed to the following factors: (1) Voxel-based Receptive Field: Voxel-based methods tend to increase the receptive field of feature points through convolutional downsampling, capturing distant semantic information with larger receptive fields but potentially missing finer local features. (2) Foreground Point Retention: In autonomous driving

scenarios, most points constitute background, while only a few points are foreground and relevant for detection. Voxel-based downsampling may lead to discarding some foreground points. (3) Lidar-generated point clouds are sparse, especially for distant, small-sized, and low-reflective objects. Constructing a 3D feature layer through voxelization exacerbates the sparsity of initially sparse feature points, making it challenging to retain geometric information. (4) Object Centroid and Feature Aggregation: Lidar point clouds often capture only the surfaces of objects, with the centroid of an object frequently far from feature points. In our proposed method: (1) Multi-scale Voxelization is employed to generate both long-range semantic information and fine-grained local features; (2) In the Multi-Scale Voxelization’s encoder process, distance weights ( $W_d$ ) are generated to preserve foreground points closer to object centroids, with weight mean operations further emphasizing foreground feature information; (3) Various levels of sparse voxel features contribute to a denser 3D feature layer with diverse semantic information; (4) Motivated by VoteNet [35], we use Center Vote to compute the offsets of deep feature points from the object’s centroid, enabling them to better aggregate features for subsequent stages. Moreover, compared to Voxel-based methods, Point-based methods typically mitigate information loss. Our method also demonstrates promising competitiveness compared to Point-based methods and the Point & Voxel-based PV-RCNN. We visualize our detection results on the KITTI dataset in Fig. 7.

To further validate the performance of our method in complex environments, we conducted comparisons with voxel-based two-stage methods (PartA2, Voxel RCNN, PV-RCNN, with PV-RCNN being a method that fuses voxels and points). We trained our model on the training set of the KITTI dataset and compared the detection accuracy under Hard conditions on the validation set. Furthermore, to assess the detection accuracy of our proposed method in sparser point cloud scenarios, we randomly discarded 40% of the point clouds in each data sample from the validation set and conducted comparisons under Moderate and Hard conditions (randomly discarding

<sup>1</sup><https://github.com/open-mmlab/OpenPCDet>

TABLE I

RESULTS OF 3D DETECTION BENCHMARKS ON THE KITTI TEST SET. ‘V’ DENOTES VOXEL-BASED METHODS. ‘P’ DENOTES POINT-BASED METHODS. ‘P+V’ DENOTES MIXED POINT-BASED AND VOXEL-BASED METHODS. ‘L’ DENOTES THE USAGE OF ONLY LIDAR DATA AS INPUT. ‘L+I’ DENOTES USING BOTH LIDAR AND IMAGE DATA AS INPUT.

Method	Type	Sens.	Car $AP_{3D}(\%)$			Pedestrian $AP_{3D}(\%)$			Cyclist $AP_{3D}(\%)$		
			Easy	Mod.	Hard	Easy	Mod.	Hard	Easy	Mod.	Hard
MV3D [36]	-	$L + I$	74.97	63.63	54.00	-	-	-	-	-	-
F-ConvNet [50]	-	$L + I$	87.36	76.39	66.69	-	-	-	-	-	-
IPOD [51]	-	$L + I$	71.40	53.46	48.34	-	-	-	-	-	-
EPNet [52]	-	$L + I$	59.81	79.28	74.50	-	-	-	-	-	-
ContFuse [53]	-	$L + I$	83.68	68.78	61.67	-	-	-	-	-	-
CT3D [54]	-	$L + I$	87.83	81.77	77.16	-	-	-	-	-	-
AVOD [37]	-	$L + I$	83.07	71.76	63.73	50.46	42.27	39.04	63.76	50.55	44.93
F-PointNet [55]	-	$L + I$	82.19	69.76	60.59	50.53	42.15	38.08	72.27	56.12	49.01
3DSSD [34]	$P$	$L$	88.36	79.57	74.55	-	-	-	-	-	-
IA-SSD [35]	$P$	$L$	88.34	80.13	75.04	46.51	39.03	35.60	78.35	61.94	55.70
STD [56]	$P$	$L$	87.95	79.71	75.09	53.29	42.49	38.55	78.69	61.59	55.30
Point-GNN [57]	$P$	$L$	88.33	79.47	74.55	54.64	44.27	40.23	82.48	64.10	56.90
Point RCNN [33]	$P$	$L$	85.94	75.76	68.32	49.43	41.78	38.63	78.58	62.73	57.74
BADet [45]	$P + V$	$L$	89.28	81.61	76.58	-	-	-	-	-	-
HVPR [44]	$P + V$	$L$	86.38	77.92	73.04	53.47	43.96	40.64	-	-	-
PV-RCNN [43]	$P + V$	$L$	92.25	81.43	76.82	52.17	43.29	40.29	78.60	63.71	57.65
SECOND [21]	$V$	$L$	83.34	72.55	65.82	-	-	-	-	-	-
Voxel RCNN [23]	$V$	$L$	90.90	81.62	77.06	-	-	-	-	-	-
VP-Net [18]	$V$	$L$	90.46	82.03	79.65	-	-	-	-	-	-
SA-SSD [25]	$V$	$L$	88.75	79.79	74.16	-	-	-	-	-	-
SECOND [21]	$V$	$L$	83.34	72.55	65.82	-	-	-	-	-	-
PartA <sup>2</sup> [28]	$V$	$L$	85.94	77.86	72.00	54.49	44.50	42.36	78.58	62.73	57.74
PointPillars [40]	$V$	$L$	82.58	74.31	68.99	51.45	41.92	38.89	77.10	58.65	51.92
H <sup>2</sup> 3D RCNN [41]	$V$	$L$	92.43	81.55	77.22	52.75	45.26	41.65	78.67	62.74	55.78
ASCNet [58]	$V$	$L$	88.48	81.67	76.93	42.00	35.76	33.69	78.41	65.10	57.87
SIEV-Net [19]	$V$	$L$	85.21	76.18	70.60	54.00	44.80	41.11	78.75	59.99	52.37
Ours	$V$	$L$	88.05	79.64	74.93	51.83	42.73	39.49	80.48	64.81	57.21

TABLE II

RESULTS ON THE KITTI VALIDATION SET (3712 SAMPLES FOR TRAINING AND 3769 SAMPLES FOR VALIDATION).

Method	Type	Hard			Mod \ Hard (Drop 0.4)		
		Car	Ped.	Cyc.	Car	Ped.	Cyc.
PV-RCNN [43]	P+V	77.86	45.02	60.96	77.35\75.55	47.90\43.48	58.70\54.95
PartA <sup>2</sup> [28]	V	78.50	44.53	<b>65.67</b>	<b>77.97</b> \73.04	48.89\42.04	60.68\57.08
Voxel RCNN [23]	V	<b>79.31</b>	48.15	64.03	77.48\75.98	49.30\43.96	61.62\56.74
Ours	V	78.43	<b>50.33</b>	63.93	77.46\74.48	<b>52.11</b> \47.08	<b>62.47</b> \57.14

40% of point clouds only during the validation phase). The detection results are shown in Table II. From Table II, it can be observed that under the Hard conditions, our method exhibits commendable detection performance for pedestrians and cyclists. Thanks to the Semantic Feature Aggregation module proposed in this paper (which constructs denser 3D feature layers using semantic feature points at different levels), our method maintains good detection accuracy under both Hard and Moderate conditions, even with the random discarding of 40% of the point clouds.

#### D. Result on ONCE Dataset

To further validate the performance of MS<sup>2</sup>3D in more complex scenarios, we conducted detections using MS<sup>2</sup>3D

on the validation set of the ONCE dataset. As shown in Table III, MS<sup>2</sup>3D maintains its competitiveness compared to other voxel-based methods. It again confirms that the proposed method can deliver substantial performance even in large-scale and intricate LiDAR scenes. In Fig. 8, we present visualized detection results on the ONCE dataset.

#### E. Ablation Experiments

In this section, we conduct ablation experiments to evaluate the three Center Vote schemes mentioned in Multi-Scale Voxelization. All experiments are performed on the same hardware with consistent parameter settings for training. The final results are evaluated on the KITTI validation set.

**Ablation Experiments with Distance Weights:** In Multi-Scale Voxelization, we introduced the method of using distance weights ( $W_d$ ) to pick out feature points more favorable for object detection and emphasize their feature information. To analyze this, we conducted experiments with and without supervised signals provided to  $W_d$  during training. Method (1) in Table III does not offer supervised signals to  $W_d$ . Method (2) involves supervising  $W_d$  through  $L_{ctr}$ , as mentioned in Multi-Scale Voxelization. Comparing the results of methods (1) and (2) in Table III, we observe that method (2) yields improved detection accuracy for both ‘Car’ and ‘Cyclist’. This is



TABLE III  
RESULTS ON THE ONCE VALIDATION SET.

Method	Type	Vehicle				Pedestrian				Cyclist				mAP
		overall	0 – 30m	30 – 50m	> 50m	overall	0 – 30m	30 – 50m	> 50m	overall	0 – 30m	30 – 50m	> 50m	
PV-RCNN [43]	$P + V$	77.77	89.39	72.55	58.64	23.50	25.61	22.84	17.27	59.37	71.66	52.58	36.17	53.55
Point RCNN [33]	$P$	52.09	74.45	40.89	16.81	4.28	6.17	2.40	0.91	29.84	46.03	20.94	5.46	28.74
PointPillars [40]	$V$	68.57	80.86	62.07	47.04	17.63	19.47	15.15	10.23	46.81	58.33	40.32	25.86	44.34
CenterPoints [62]	$V$	66.79	80.10	59.55	43.39	49.90	56.24	42.61	26.27	63.45	74.28	57.94	41.48	60.05
SECOND [21]	$V$	71.19	84.04	63.02	47.25	26.44	29.33	24.05	18.05	58.04	69.69	52.43	34.61	51.86
Ours	$V$	74.08	86.09	67.05	51.27	26.84	32.33	20.67	12.8	56.12	69.94	47.31	28.64	52.35

TABLE IV

RESULTS OF ABLATION EXPERIMENTS. THE EVALUATION IS CONDUCTED ON THE KITTI VALIDATION SET, USING 3D AP WITH RECALLS@40 UNDER THE MODERATE SETTING AS THE ACCURACY METRIC. IN THE TABLE, ‘CENTERNESS’ DENOTES THE USE OF  $L_{ctr}$  FOR SUPERVISING  $W_d$ ; ‘MV-VOTE’ DENOTES THE CENTER VOTE APPLIED TO THE LAST LAYER OF MULTI-SCALE VOXELIZATION; ‘ALL-VOTE’ DENOTES THE CENTER VOTE APPLIED TO ALL FEATURE POINTS IN THE 3D FEATURE LAYER; ‘ $V_i$ -VOTE’ DENOTES THE CENTER VOTE APPLIED TO THE  $V_i$  IN THE 3D FEATURE LAYER; ‘ $F_i$ -VOTE’ DENOTES THE CENTER VOTE APPLIED TO THE  $F_i$  IN THE 3D FEATURE LAYER. THE BOLDED PORTIONS REPRESENT THE BEST RESULTS.

Method	Centerness	MV-Vote	All-Vote	$V_i$ -Vote	$F_i$ -Vote	Car Mod. (IoU = 0.7)	Ped. Mod. (IoU = 0.5)	Cyc. Mod. (IoU = 0.5)
(1)	-	-	-	-	-	78.69	<b>58.02</b>	63.09
(2)	✓	-	-	-	-	82.34	57.49	64.00
(3)	✓	✓	-	-	-	82.53	58.13	64.34
(4)	✓	✓	✓	-	-	79.96	56.93	62.36
(5)	✓	✓	-	✓	-	81.36	55.42	63.79
(6)	✓	✓	-	-	✓	<b>82.70</b>	57.87	<b>69.84</b>

because supervised signals guide  $W_d$  to assign greater weights to feature points closer to instance centers, and during Multi-Scale Voxelization’s sampling process, it selects foreground points as much as possible.

**Ablation Experiments with Center Voting in Multi-Scale Voxelization:** In Multi-Scale Voxelization, we proposed conducting Center Vote on the last layer ( $V_4$ ) of Multi-Scale Voxelization. We carried out experiments to analyze the effects of performing Center Vote. Method (2) in Table IV indicates no Center Vote, while method (2) performs Center Vote on  $V_4$ . By comparing the experimental results, we observe that method (3) exhibits a slight improvement over method (2). This enhancement is attributed to the rich semantic features contained in  $V_4$ , combined with its substantial receptive field. Center Vote on  $V_4$  enables it to shift closer to the object’s center of mass, facilitating subsequent RPN network-generated region proposals.

**Ablation Experiments with Semantic Feature Aggregation:** In Semantic Feature Aggregation, we presented three Center Vote schemes for the 3D feature layer. Method (3) involves no Center Vote on the 3D feature layer; method (4) applies Center Vote to all feature points within the 3D feature layer; method (5) conducts Center Vote on feature points ( $V_i$ ) from Multi-Scale Voxelization within the 3D feature layer; method (6) performs Center Vote on feature points ( $F_i$ ) from the 3D Encoder within the 3D feature layer. Comparing the experimental results in Table IV, we observe that method (6) demonstrates a significant improvement over method (3), while methods (4) and (5) exhibit worse detection results than method (3). As illustrated in Figure 5, applying Center Vote

to all feature points in method (4) leads to severe distortion of object geometry. Particularly in the z-axis direction, the 3D feature layer constructed by method (4) shifts all z-axis points onto the plane of the object’s center of mass, thus considerably compromising spatial information in the z-axis direction. Method (5) shows improved detection accuracy compared to method (4), but its 3D feature layer construction still struggles to capture object geometry well. Method (6), which applies Center Vote only to  $F_i$ , both guide the deep-layer feature  $F_i$  with rich semantic information to shift closer to the object’s center of mass and retain object geometry to the greatest extent possible.

## V. CONCLUSION

In this paper, we propose a two-stage detection method named MS<sup>2</sup>3D, which constructs the 3D feature layer using multi-scale semantic feature points. Considering the issue of information loss in fine-grained feature details during the downsampling process of Voxel-based methods, we propose the Multi-Scale Voxelization. This method employs small-sized voxels to extract localized fine-grained features and large-sized voxels to capture coarse-grained long-range features. Moreover, we propose Semantic Feature Aggregation to address the sparsity of the 3D feature layer and the challenge of most feature points being concentrated on object surfaces. This approach facilitates the construction of a dense 3D feature layer from feature points at various scales, and it employs Center Vote on deep-level feature points enriched with semantic information, ensuring their proximity to the object’s center of mass. In the subsequent experimental sections, we comprehensively demonstrate the effectiveness of the proposed approach presented in this paper.

## REFERENCES

- [1] A. Bochkovskiy, C.-Y. Wang, and H.-Y. M. Liao, “Yolov4: Optimal speed and accuracy of object detection,” *arXiv preprint arXiv:2004.10934*, 2020.
- [2] W. Liu, D. Anguelov, D. Erhan, C. Szegedy, S. Reed, C.-Y. Fu, and A. C. Berg, “Ssd: Single shot multibox detector,” in *Computer Vision—ECCV 2016: 14th European Conference, Amsterdam, The Netherlands, October 11–14, 2016, Proceedings, Part I 14*. Springer, 2016, pp. 21–37.
- [3] S. Ren, K. He, R. Girshick, and J. Sun, “Faster r-cnn: Towards real-time object detection with region proposal networks,” *Advances in neural information processing systems*, vol. 28, 2015.
- [4] T. Gao, Q. Niu, J. Zhang, T. Chen, S. Mei, and A. Jubair, “Global to local: A scale-aware network for remote sensing object detection,” *IEEE Transactions on Geoscience and Remote Sensing*, vol. 61, pp. 1–14, 2023.

- [5] A. Bulletti, G. Borgioli, M. Calzolari, L. Capineri, and M. Mazzone, "Acoustoseismic method for buried-object detection by means of surface-acceleration measurements and audio facilities," *IEEE Transactions on Geoscience and Remote Sensing*, vol. 48, no. 8, pp. 3134–3138, 2010.
- [6] D. Yu and S. Ji, "A new spatial-oriented object detection framework for remote sensing images," *IEEE Transactions on Geoscience and Remote Sensing*, vol. 60, pp. 1–16, 2022.
- [7] M. Cherniakov and L. Donskoi, "Frequency band selection of radars for buried object detection," *IEEE Transactions on Geoscience and Remote Sensing*, vol. 37, no. 2, pp. 838–845, 1999.
- [8] W. Ma, N. Li, H. Zhu, L. Jiao, X. Tang, Y. Guo, and B. Hou, "Feature split-merge-enhancement network for remote sensing object detection," *IEEE Transactions on Geoscience and Remote Sensing*, vol. 60, pp. 1–17, 2022.
- [9] J. Sun, L. Chen, Y. Xie, S. Zhang, Q. Jiang, X. Zhou, and H. Bao, "Disp r-cnn: Stereo 3d object detection via shape prior guided instance disparity estimation," in *Proceedings of the IEEE/CVF conference on computer vision and pattern recognition*, 2020, pp. 10 548–10 557.
- [10] Y. Chen, S. Liu, X. Shen, and J. Jia, "Dsgn: Deep stereo geometry network for 3d object detection," in *Proceedings of the IEEE/CVF conference on computer vision and pattern recognition*, 2020, pp. 12 536–12 545.
- [11] J.-R. Chang and Y.-S. Chen, "Pyramid stereo matching network," in *Proceedings of the IEEE conference on computer vision and pattern recognition*, 2018, pp. 5410–5418.
- [12] P. Li, X. Chen, and S. Shen, "Stereo r-cnn based 3d object detection for autonomous driving," in *Proceedings of the IEEE/CVF Conference on Computer Vision and Pattern Recognition*, 2019, pp. 7644–7652.
- [13] X. Chen, K. Kundu, Y. Zhu, A. G. Berneshawi, H. Ma, S. Fidler, and R. Urtasun, "3d object proposals for accurate object class detection," *Advances in neural information processing systems*, vol. 28, 2015.
- [14] Z. Deng and L. Jan Latecki, "Amodal detection of 3d objects: Inferring 3d bounding boxes from 2d ones in rgb-depth images," in *Proceedings of the IEEE Conference on Computer Vision and Pattern Recognition*, 2017, pp. 5762–5770.
- [15] D. Xu, W. Ouyang, E. Ricci, X. Wang, and N. Sebe, "Learning cross-modal deep representations for robust pedestrian detection," in *Proceedings of the IEEE conference on computer vision and pattern recognition*, 2017, pp. 5363–5371.
- [16] S. Gupta, R. Girshick, P. Arbeláez, and J. Malik, "Learning rich features from rgb-d images for object detection and segmentation," in *Computer Vision—ECCV 2014: 13th European Conference, Zurich, Switzerland, September 6–12, 2014, Proceedings, Part VII 13*. Springer, 2014, pp. 345–360.
- [17] Y. Shao, Z. Sun, A. Tan, and T. Yan, "Efficient three-dimensional point cloud object detection based on improved complex-yolo," *Frontiers in Neurorobotics*, vol. 17, p. 1092564, 2023.
- [18] Z. Song, H. Wei, C. Jia, Y. Xia, X. Li, and C. Zhang, "Vp-net: Voxels as points for 3-d object detection," *IEEE Transactions on Geoscience and Remote Sensing*, vol. 61, pp. 1–12, 2023.
- [19] C. Yu, J. Lei, B. Peng, H. Shen, and Q. Huang, "Siev-net: A structure-information enhanced voxel network for 3d object detection from lidar point clouds," *IEEE Transactions on Geoscience and Remote Sensing*, vol. 60, pp. 1–11, 2022.
- [20] C. R. Qi, H. Su, K. Mo, and L. J. Guibas, "Pointnet: Deep learning on point sets for 3d classification and segmentation," in *Proceedings of the IEEE conference on computer vision and pattern recognition*, 2017, pp. 652–660.
- [21] Y. Yan, Y. Mao, and B. Li, "Second: Sparsely embedded convolutional detection," *Sensors*, vol. 18, no. 10, p. 3337, 2018.
- [22] Y. Zhou and O. Tuzel, "Voxelnet: End-to-end learning for point cloud based 3d object detection," in *Proceedings of the IEEE conference on computer vision and pattern recognition*, 2018, pp. 4490–4499.
- [23] J. Deng, S. Shi, P. Li, W. Zhou, Y. Zhang, and H. Li, "Voxel r-cnn: Towards high performance voxel-based 3d object detection," in *Proceedings of the AAAI Conference on Artificial Intelligence*, vol. 35, no. 2, 2021, pp. 1201–1209.
- [24] C. R. Qi, O. Litany, K. He, and L. J. Guibas, "Deep hough voting for 3d object detection in point clouds," in *proceedings of the IEEE/CVF International Conference on Computer Vision*, 2019, pp. 9277–9286.
- [25] C. He, H. Zeng, J. Huang, X.-S. Hua, and L. Zhang, "Structure aware single-stage 3d object detection from point cloud," in *Proceedings of the IEEE/CVF conference on computer vision and pattern recognition*, 2020, pp. 11 873–11 882.
- [26] W. Zheng, W. Tang, S. Chen, L. Jiang, and C.-W. Fu, "Cia-ssd: Confident iou-aware single-stage object detector from point cloud," in *Proceedings of the AAAI conference on artificial intelligence*, vol. 35, no. 4, 2021, pp. 3555–3562.
- [27] M. Ye, S. Xu, and T. Cao, "Hvnet: Hybrid voxel network for lidar based 3d object detection," in *Proceedings of the IEEE/CVF conference on computer vision and pattern recognition*, 2020, pp. 1631–1640.
- [28] S. Shi, Z. Wang, J. Shi, X. Wang, and H. Li, "From points to parts: 3d object detection from point cloud with part-aware and part-aggregation network," *IEEE transactions on pattern analysis and machine intelligence*, vol. 43, no. 8, pp. 2647–2664, 2020.
- [29] S. Thakur and J. Peethambaran, "Dynamic edge weights in graph neural networks for 3d object detection," *arXiv preprint arXiv:2009.08253*, 2020.
- [30] W. Yue, S. Yongbin, L. Ziwei, S. E. Sarma, M. M. Bronstein, and J. M. Solomon, "Dynamic graph cnn for learning on point clouds," *ACM Transactions on Graphics (TOG)*, vol. 38, no. 5, 2019.
- [31] C. R. Qi, L. Yi, H. Su, and L. J. Guibas, "Pointnet++: Deep hierarchical feature learning on point sets in a metric space," *Advances in neural information processing systems*, vol. 30, 2017.
- [32] Y. Liu, B. Fan, S. Xiang, and C. Pan, "Relation-shape convolutional neural network for point cloud analysis," in *Proceedings of the IEEE/CVF conference on computer vision and pattern recognition*, 2019, pp. 8895–8904.
- [33] S. Shi, X. Wang, and H. Li, "Pointcnn: 3d object proposal generation and detection from point cloud," in *Proceedings of the IEEE/CVF conference on computer vision and pattern recognition*, 2019, pp. 770–779.
- [34] Z. Yang, Y. Sun, S. Liu, and J. Jia, "3dssd: Point-based 3d single stage object detector," in *Proceedings of the IEEE/CVF conference on computer vision and pattern recognition*, 2020, pp. 11 040–11 048.
- [35] Y. Zhang, Q. Hu, G. Xu, Y. Ma, J. Wan, and Y. Guo, "Not all points are equal: Learning highly efficient point-based detectors for 3d lidar point clouds," in *Proceedings of the IEEE/CVF Conference on Computer Vision and Pattern Recognition*, 2022, pp. 18 953–18 962.
- [36] X. Chen, H. Ma, J. Wan, B. Li, and T. Xia, "Multi-view 3d object detection network for autonomous driving," in *Proceedings of the IEEE conference on Computer Vision and Pattern Recognition*, 2017, pp. 1907–1915.
- [37] J. Ku, M. Mozifian, J. Lee, A. Harakeh, and S. L. Waslander, "Joint 3d proposal generation and object detection from view aggregation," in *2018 IEEE/RSJ International Conference on Intelligent Robots and Systems (IROS)*. IEEE, 2018, pp. 1–8.
- [38] M. Simony, S. Milzy, K. Amendy, and H.-M. Gross, "Complex-yolo: An euler-region-proposal for real-time 3d object detection on point clouds," in *Proceedings of the European conference on computer vision (ECCV) workshops*, 2018, pp. 0–0.
- [39] W. Ali, S. Abdelkarim, M. Zidan, M. Zahran, and A. El Sallab, "Yolo3d: End-to-end real-time 3d oriented object bounding box detection from lidar point cloud," in *Proceedings of the European conference on computer vision (ECCV) workshops*, 2018, pp. 0–0.
- [40] A. H. Lang, S. Vora, H. Caesar, L. Zhou, J. Yang, and O. Beijbom, "Pointpillars: Fast encoders for object detection from point clouds," in *Proceedings of the IEEE/CVF conference on computer vision and pattern recognition*, 2019, pp. 12 697–12 705.
- [41] J. Deng, W. Zhou, Y. Zhang, and H. Li, "From multi-view to hollow-3d: Hallucinated hollow-3d r-cnn for 3d object detection," *IEEE Transactions on Circuits and Systems for Video Technology*, vol. 31, no. 12, pp. 4722–4734, 2021.
- [42] Z. Liu, H. Tang, Y. Lin, and S. Han, "Point-voxel cnn for efficient 3d deep learning," *Advances in Neural Information Processing Systems*, vol. 32, 2019.
- [43] S. Shi, C. Guo, L. Jiang, Z. Wang, J. Shi, X. Wang, and H. Li, "Pv-rccn: Point-voxel feature set abstraction for 3d object detection," in *Proceedings of the IEEE/CVF conference on computer vision and pattern recognition*, 2020, pp. 10 529–10 538.
- [44] J. Noh, S. Lee, and B. Ham, "Hvpr: Hybrid voxel-point representation for single-stage 3d object detection," in *Proceedings of the IEEE/CVF conference on computer vision and pattern recognition*, 2021, pp. 14 605–14 614.
- [45] R. Qian, X. Lai, and X. Li, "Badet: Boundary-aware 3d object detection from point clouds," *Pattern Recognition*, vol. 125, p. 108524, 2022.
- [46] Y. Shao, A. Tan, Z. Sun, E. Zheng, and T. Yan, "Pv-ssd: A projection and voxel-based double branch single-stage 3d object detector," *arXiv preprint arXiv:2308.06791*, 2023.
- [47] Y. Zhou, P. Sun, Y. Zhang, D. Anguelov, J. Gao, T. Ouyang, J. Guo, J. Ngiam, and V. Vasudevan, "End-to-end multi-view fusion for 3d object detection in lidar point clouds," in *Conference on Robot Learning*. PMLR, 2020, pp. 923–932.

- [48] A. Geiger, P. Lenz, and R. Urtasun, "Are we ready for autonomous driving? the kitti vision benchmark suite," in *2012 IEEE conference on computer vision and pattern recognition*. IEEE, 2012, pp. 3354–3361.
- [49] J. Mao, M. Niu, C. Jiang, H. Liang, J. Chen, X. Liang, Y. Li, C. Ye, W. Zhang, Z. Li *et al.*, "One million scenes for autonomous driving: Once dataset," *arXiv preprint arXiv:2106.11037*, 2021.
- [50] Z. Wang and K. Jia, "Frustum convnet: Sliding frustums to aggregate local point-wise features for amodal 3d object detection," in *2019 IEEE/RSJ International Conference on Intelligent Robots and Systems (IROS)*. IEEE, 2019, pp. 1742–1749.
- [51] Z. Yang, Y. Sun, S. Liu, X. Shen, and J. Jia, "Ipod: Intensive point-based object detector for point cloud," *arXiv preprint arXiv:1812.05276*, 2018.
- [52] T. Huang, Z. Liu, X. Chen, and X. Bai, "Epnet: Enhancing point features with image semantics for 3d object detection," in *Computer Vision—ECCV 2020: 16th European Conference, Glasgow, UK, August 23–28, 2020, Proceedings, Part XV 16*. Springer, 2020, pp. 35–52.
- [53] M. Liang, B. Yang, S. Wang, and R. Urtasun, "Deep continuous fusion for multi-sensor 3d object detection," in *Proceedings of the European conference on computer vision (ECCV)*, 2018, pp. 641–656.
- [54] H. Sheng, S. Cai, Y. Liu, B. Deng, J. Huang, X.-S. Hua, and M.-J. Zhao, "Improving 3d object detection with channel-wise transformer," in *Proceedings of the IEEE/CVF International Conference on Computer Vision*, 2021, pp. 2743–2752.
- [55] C. R. Qi, W. Liu, C. Wu, H. Su, and L. J. Guibas, "Frustum pointnets for 3d object detection from rgb-d data," in *Proceedings of the IEEE conference on computer vision and pattern recognition*, 2018, pp. 918–927.
- [56] Z. Yang, Y. Sun, S. Liu, X. Shen, and J. Jia, "Std: Sparse-to-dense 3d object detector for point cloud," in *Proceedings of the IEEE/CVF international conference on computer vision*, 2019, pp. 1951–1960.
- [57] W. Shi and R. Rajkumar, "Point-gnn: Graph neural network for 3d object detection in a point cloud," in *Proceedings of the IEEE/CVF conference on computer vision and pattern recognition*, 2020, pp. 1711–1719.
- [58] G. Tong, H. Peng, Y. Shao, Q. Yin, and Z. Li, "Ascnet: 3d object detection from point cloud based on adaptive spatial context features," *Neurocomputing*, vol. 475, pp. 89–101, 2022.
- [59] B. Yang, W. Luo, and R. Urtasun, "Pixor: Real-time 3d object detection from point clouds," in *Proceedings of the IEEE conference on Computer Vision and Pattern Recognition*, 2018, pp. 7652–7660.
- [60] D. P. Kingma and J. Ba, "Adam: A method for stochastic optimization," *arXiv preprint arXiv:1412.6980*, 2014.
- [61] L. N. Smith and N. Topin, "Super-convergence: Very fast training of neural networks using large learning rates," in *Artificial intelligence and machine learning for multi-domain operations applications*, vol. 11006. SPIE, 2019, pp. 369–386.
- [62] T. Yin, X. Zhou, and P. Krahenbuhl, "Center-based 3d object detection and tracking," in *Proceedings of the IEEE/CVF conference on computer vision and pattern recognition*, 2021, pp. 11 784–11 793.